Materials Science & Engineering A 648 (2015) 183–192

Contents lists available at ScienceDirect

Materials Science & Engineering A

journal homepage: www.elsevier.com/locate/msea

Non-equiatomic high entropy alloys: Approach towards rapid alloy screening and property-oriented design

K.G. Pradeep [a,b], C.C. Tasan [a,*], M.J. Yao [a], Y. Deng [a,c], H. Springer [a], D. Raabe [a,*]

[a] Max-Planck-Institut für Eisenforschung GmbH, Max-Planck-str.1, 40237 Düsseldorf, Germany
[b] Materials Chemistry, RWTH Aachen University, Kopernikusstr.10, 52074 Aachen, Germany
[c] Department of Engineering Design and Materials, Norwegian University of Science and Technology, No-7491 Trondheim, Norway

ARTICLE INFO

Article history:
Received 25 July 2015
Received in revised form
3 September 2015
Accepted 3 September 2015
Available online 10 September 2015

Keywords:
Non-equiatomic
Solid solution
CoCrFeMnNi
Alloy design
Single phase

ABSTRACT

The high entropy alloy (HEA) concept has triggered a renewed interest in alloy design, even though some aspects of the underlying thermodynamic concepts are still under debate. This study addresses the shortcomings of this alloy design strategy with the aim to open up new directions of HEA research targeting specifically non-equiatomic yet massively alloyed compositions. We propose that a wide range of massive single phase solid solutions could be designed by including non-equiatomic variants. It is demonstrated by introducing a set of novel non-equiatomic multi-component CoCrFeMnNi alloys produced by metallurgical rapid alloy prototyping. Despite the reduced configurational entropy, detailed characterization of these materials reveals a strong resemblance to the well-studied equiatomic single phase HEA: The microstructure of these novel alloys exhibits a random distribution of alloying elements (confirmed by Energy-Dispersive Spectroscopy and Atom Probe Tomography) in a single face-centered-cubic phase (confirmed by X-ray Diffraction and Electron Backscatter Diffraction), which deforms through planar slip (confirmed by Electron-Channeling Contrast Imaging) and leads to excellent ductility (confirmed by uniaxial tensile tests). This approach widens the field of HEAs to non-equiatomic multi-component alloys since the concept enables to tailor the stacking fault energy and associated transformation phenomena which act as main mechanisms to design useful strain hardening behavior.

1. Introduction

The High Entropy Alloy (HEA) concept has attracted significant interest in recent years due to the novelty of the underlying alloy design principle and the promising mechanical properties of the massive solid solution microstructures [1,2]. In general, the concept inherits the idea of producing bulk crystalline alloys composed of multiple components being added in proportions that are far beyond their binary solid solubility limits, yet yielding a single phase solid solution [3,4]. While in some cases the solid solutions formed possess simple crystal structures such as face-centered cubic (fcc) and body centered cubic (bcc) [5,6] and fulfill the expectations of combining high strength with good ductility [7], these successful cases constitute only a very small fraction of the significant efforts to experimentally obtain such single phase solid solutions. The underlying reason for such limited success is the very nature of the proposed alloy design strategy, which relies completely on the maximization of the configurational entropy [8–11]. The original HEA approach thus imposes the constraint of achieving this through equiatomic ratios of multiple alloying principal elements [1,12]. A limiting criterion of this type has failed to produce consistently the desired single phase solid solution forming compositions, resulting in the emergence of only a handful of equiatomic HEAs forming single phase solid solutions [3,13]. The most well-known of these is the equiatomic CoCrFeMnNi introduced by Cantor et al. [3,14–16] which forms a single fcc phase solid solution and exhibits excellent room temperature and cryogenic mechanical properties [17,18].

The present work aims at exploring the inherent flexibility involved in HEA design which would enable to overcome the limitations of HEA design concept. Following such an objective three distinct non-equiatomic single phase HEAs namely, $Fe_{40}Mn_{27}Ni_{26}Co_5Cr_2$, $Fe_{40}Mn_{40}Co_{10}Cr_{10}$ and $Fe_{37}Mn_{45}Co_9Cr_9$ (all in at%) were introduced by the authors recently [19–21], which exhibit exceptional stability and tensile properties. In all of these cases, even though the major constituents of the proposed non-equiatomic HEA are primarily the same as that of the alloy proposed by Cantor et al., the constituent proportions differ quite significantly, thus deviating from the existing HEA design

* Corresponding authors.
E-mail addresses: c.tasan@mpie.de (C.C. Tasan), d.raabe@mpie.de (D. Raabe).

http://dx.doi.org/10.1016/j.msea.2015.09.010
0921-5093/

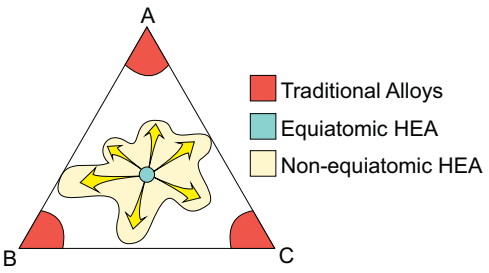

Fig. 1. A schematic comparison of traditional alloys with one base element and minor alloying additions, high entropy alloys with equiatomic compositions of all alloying elements, and non-equiatomic – yet still massively alloyed-high entropy alloys, on the isothermal cross section of a ternary phase diagram. The relaxation of the high entropy alloy criteria to include non-equiatomic compositions greatly expands the compositional ranges that can be probed and the associated accessible properties.

principles. In spite of the deviation, random single phase solid solution microstructures are successfully achieved. The recent investigation of Otto et al. demonstrated the weak dependence of single phase solid solution formability on configurational entropy [22]. Also, other works revealed that the configurational entropy curve of such materials assumes a rather flat shape so that a wide range of compositions outside of the equiatomic structure yield similar entropy values [19–21]. These results clearly show that alloy design approaches expanding towards non-equiatomic compositions have a great potential in opening up the applicability of HEAs for future applications as sketched in Fig. 1.

To demonstrate the significance of this concept, we i) introduce a series of such non-equiatomic high entropy alloys with varied chemical compositions; ii) demonstrate that a single phase solid solution is achieved in each of the introduced cases; iii) validate the stability of all those single phase solid solutions at elevated temperatures; and iv) investigate the mechanical properties in terms of bulk hardness and by tensile testing.

2. Experimental

In order to meet the above mentioned objectives, one of the previously introduced non-equiatomic alloys, namely, $Fe_{40}Mn_{27}Ni_{26}Co_5Cr_2$ (at%), is used as a starting material system. A detailed analysis by CALPHAD approach predicted that this multi-component system could retain the high temperature FCC phase upon quenching to room temperature [23]. Hence, compositional variations of the $Fe_{(64-x)}Mn_xNi_{27.7\pm1.3}Co_{5.6\pm0.3}Cr_{2.3\pm0.1}$ (at%) system with 5 different variants in $x=21$, 24, 27, 34, 38 are investigated and are designated as 21Mn, 24Mn, 27Mn, 34Mn and 38Mn alloys, as shown in Table 1 respectively. Note that various physical, thermodynamic and electronic parameters are also shown here, which will be discussed later in the discussion.

In order to understand the effect of alloy composition on the phase formation, microstructure evolution and the resulting mechanical properties of this system, an in-house developed combinatorial rapid alloy prototyping (RAP) methodology is employed [23,28]. This approach enables widely varying compositions to be metallurgically produced from a single master cast. The corresponding high purity raw metals (purity > 99.8%) were induction melted in a vacuum furnace maintained at an Argon atmosphere of 400 mbar pressure. In order to eliminate the typical cast-structures and to ensure microstructural homogeneity, hot-rolling was carried out on all as-cast blocks at 900 °C to 50% thickness reduction (from 10 mm to 5 mm) followed by homogenization at 1200 °C for 2 h in Ar atmosphere and water quenching. Microstructural characterization confirmed that the solidification structures were fully removed. Further grain refinement for mechanical property optimization was carried out through cold-rolling to 64% thickness reduction and subsequent annealing at 900 °C in Ar atmosphere for different holding times ranging from 5–120 min.

The preliminary phase formation and thermal stability characterization were carried out using X-ray diffraction (XRD) and differential scanning calorimetry (DSC). XRD measurements were carried out on a Huber-2 goniometer where the samples were exposed to Co Kα radiation ($\lambda=1.79$ Å). The Metero0D detector probed the 2θ range from 0° to 120° at a step size of $\Delta 2\theta=0.05°$. DSC experiments were performed in a SETARAM Setsys 16/18 device between 20 °C and 1300 °C at different rates (5–10 K min^{-1}) in Ar atmosphere. Microstructure characterization was carried out at all stages, i.e. on as-cast, hot rolled, homogenized, cold rolled and recrystallized samples. Emphasis is placed here on the homogenized, as cold rolled and subsequent annealed states. Secondary electron (SE) imaging, energy-dispersive X-ray spectroscopy (EDX) and electron backscatter diffraction (EBSD) were performed in a 6500F JEOL field emission gun-scanning electron microscope (FEG-SEM) equipped with an EDAX software and TSL OIM EBSD acquisition and analysis system. While the chemical homogeneity at micron-scale was investigated using EDX, the elemental distribution at the atomic scale across grain boundaries (GB) was studied using a local electrode atom probe (LEAP™ 3000X HR (Cameca Instruments)). Data analysis was performed using IVAS 3.6.8 software. Atom Probe Tomography (APT) specimens were target prepared from EBSD determined GBs using a FEI Helios Nanolab 600i dual-beam focused ion beam (FIB) following the procedures described in Ref. [29].

Mechanical properties of the homogenized, cold-rolled and recrystallized states were evaluated at room temperature on a Kammrath and Weiss GmbH tensile stage. Dog-bone-shaped specimens with gauge geometry of 4 mm × 2 mm × 1 mm were deformed at an initial strain rate of 2.5×10^{-3} s^{-1}. Prior to tensile deformation, one of the surfaces of the samples was metallographically polished for the deformation trace analysis, while a speckle pattern was applied to the opposite surface for strain measurement. The latter was carried out by digital image correlation (DIC) analysis (Aramis from GOM GmbH). In order to reveal the active deformation mechanisms, the microstructure of homogenized samples were investigated after the tensile tests. The imaging of the surface deformation features was carried out by employing the multi-focus imaging function of a Leica DM 4000M optical microscope (OM). The deformation induced

Table 1
Physical, thermodynamic and electronic parameters calculated for x-Mn alloys in comparison with the equiatomic composition.

x-Mn (at%)	Composition (at%)	δ [24] (%)	ΔH_{mix} [24] (kJ/mol)	ΔS_{conf} [25] (J/K · mol)	VEC [26]	e/a [27]	Ω [25]
21Mn	$Fe_{42.2}Mn_{20.7}Ni_{28.9}Co_{5.9}Cr_{2.3}$	4.16	−3.44	10.83	8.38	1.98	5.45
24Mn	$Fe_{41.1}Mn_{24.1}Ni_{27.1}Co_{5.5}Cr_{2.2}$	4.40	−3.52	10.89	8.31	1.98	5.32
27Mn	$Fe_{40.0}Mn_{27.0}Ni_{25.7}Co_{5.2}Cr_{2.1}$	4.58	−3.56	10.84	8.25	1.96	5.21
34Mn	$Fe_{29.4}Mn_{33.9}Ni_{28.5}Co_{5.8}Cr_{2.4}$	4.95	−4.40	11.13	8.24	2.00	4.70
38Mn	$Fe_{25.7}Mn_{37.6}Ni_{28.5}Co_{5.8}Cr_{2.4}$	4.92	−4.17	11.05	8.21	2.00	4.48
EA	$Fe_{20}Mn_{20}Ni_{20}Co_{20}Cr_{20}$	4.19	−4.16	13.38	8.00	1.80	5.76

evolution of dislocation structures was studied on the cross-section of fractured samples (at positions of known local strain levels) by employing electron channeling contrast imaging (ECCI) [30,31] in a Zeiss Merlin SEM. Hardness measurements were performed on a LECO M-400-H1 microhardness tester using a diamond pyramid indenter with an applied load of 1 kg. The reported values are averages of minimum 12 indentation measurements sufficiently spaced to avoid mechanical influence.

3. Results

3.1. Microstructure and phase stability

3.1.1. As-cast state

The as-cast microstructures of the 21Mn, 27Mn and 38Mn alloys are shown in Fig. 2(a). Typical cast dendrites and heterogeneities in the grain structure are present. Correspondingly, Fig. 2 (b) shows the XRD patterns of all the x-Mn alloys with varied peak intensities indicating the presence of differently oriented or textured grains in the as-cast state. However, in all cases, the XRD peaks clearly correspond to a single fcc phase. Within the experimental limits, the peak positions of all alloys show a very gradual angular shift towards lower 2θ values indicating a slight increase in lattice parameter (from ~3.60 Å at 21Mn to ~3.62 Å at 38Mn) with increasing Mn concentration.

In order to validate the stability of the as-cast fcc solid solution, DSC measurements were performed at a heating rate of 10 K min^{-1} for all the x-Mn alloys as shown in Fig. 2(c). The absence of both, exothermic and endothermic phase transformation peaks indicate that the varying x-Mn alloys are highly stable at all annealing temperatures prior to melting at around 1250 °C. For the case of the 27Mn alloy, additional DSC trace with an even lower heating rate of 5 K min^{-1} was performed as shown in Fig. 2 (c) which further confirms the absence of phase transformations and the stability of as-formed single fcc solid solution.

3.1.2. Homogenized state

Fig. 3 shows the EBSD and EDX characterization of the microstructures of the homogenized 21Mn, 27Mn and 38Mn alloys as representatives for all the five alloys. The EBSD phase map shown in Fig. 3((a1)–(c1)) further confirms the presence of single fcc solid solution phase after homogenization treatment. Some unindexed points (black dots) are observed in Fig. 3((a1)–(c1)) due to the presence of cast porosities or MnO particles along GBs. The inverse pole figure (IPF) maps in Fig. 3((a2)–(c2)) reveal the presence of fully recrystallized equi-axed grains with average grain sizes of ~50–60 μm as shown in the histogram. Annealing twins are also observed in the homogenized state. In order to ensure chemical homogeneity of the fcc solid solution phase, elemental EDX maps in conjunction with EBSD scans are shown in Fig. 3((a3)–(c3)). All elements are homogeneously distributed within the representative large scan area, except for slight segregation of Ni in the 38Mn alloy. Also local Mn enrichments are observed for the 27Mn and 38Mn alloys due to MnO formation, typical for high-Mn alloys [17,32].

Additionally, the local chemical homogeneity at the atomic scale within the grains and also across grain boundaries have been investigated using APT [5]. As a representative for all the x-Mn alloys, the case of the median 27Mn alloy where a specific twin boundary (indicated by white arrow in the EBSD IPF map of Fig. 4 (a) was investigated as shown in Fig. 4. All the constituent elements are homogeneously distributed as shown in Fig. 4(b). Binomial frequency distribution analysis (Fig. 4(c)) further confirms the random distribution of alloying elements with the normalized parameter μ returning values close to 0 indicating complete randomness [33,34].

The preferential segregation of carbon at the GB (red dotted lines in Fig. 4(d) showing both, cross-section and top views), which is present as impurity in the alloy (~0.039 at%), enables us to infer that the GB of interest was indeed present in the volume probed by APT. The 1D concentration profile (Fig. 4(e)) taken along a 10 nm diameter cylindrical region of interest (in Fig. 4(d)) shows

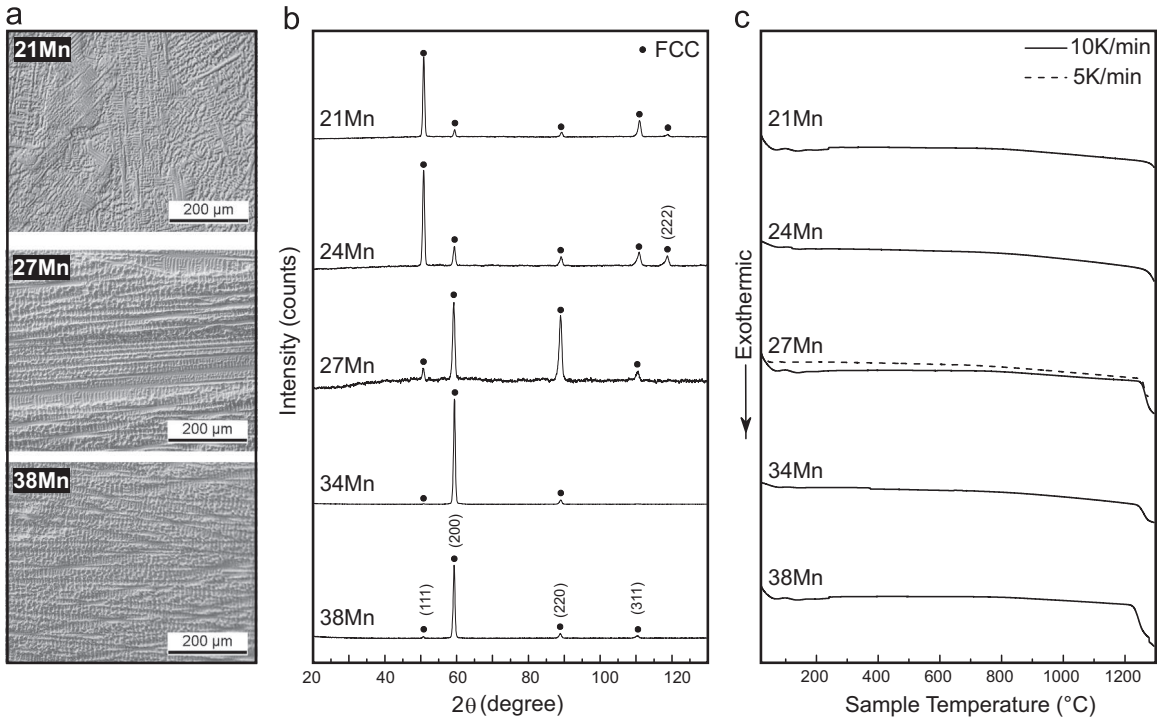

Fig. 2. (a) Optical microscopy images displaying the typical as-cast dendritic structure (similar features are observed also for the 24Mn and 34Mn alloys); (b) corresponding XRD pattern indicating the presence of a single phase solid solution with increasing lattice parameter from 3.6 Å at 21Mn to 3.62 Å for 38Mn compositions. (c) DSC traces of all the x-Mn as cast alloys exhibiting the stability of the as-formed single phase solution until melting.

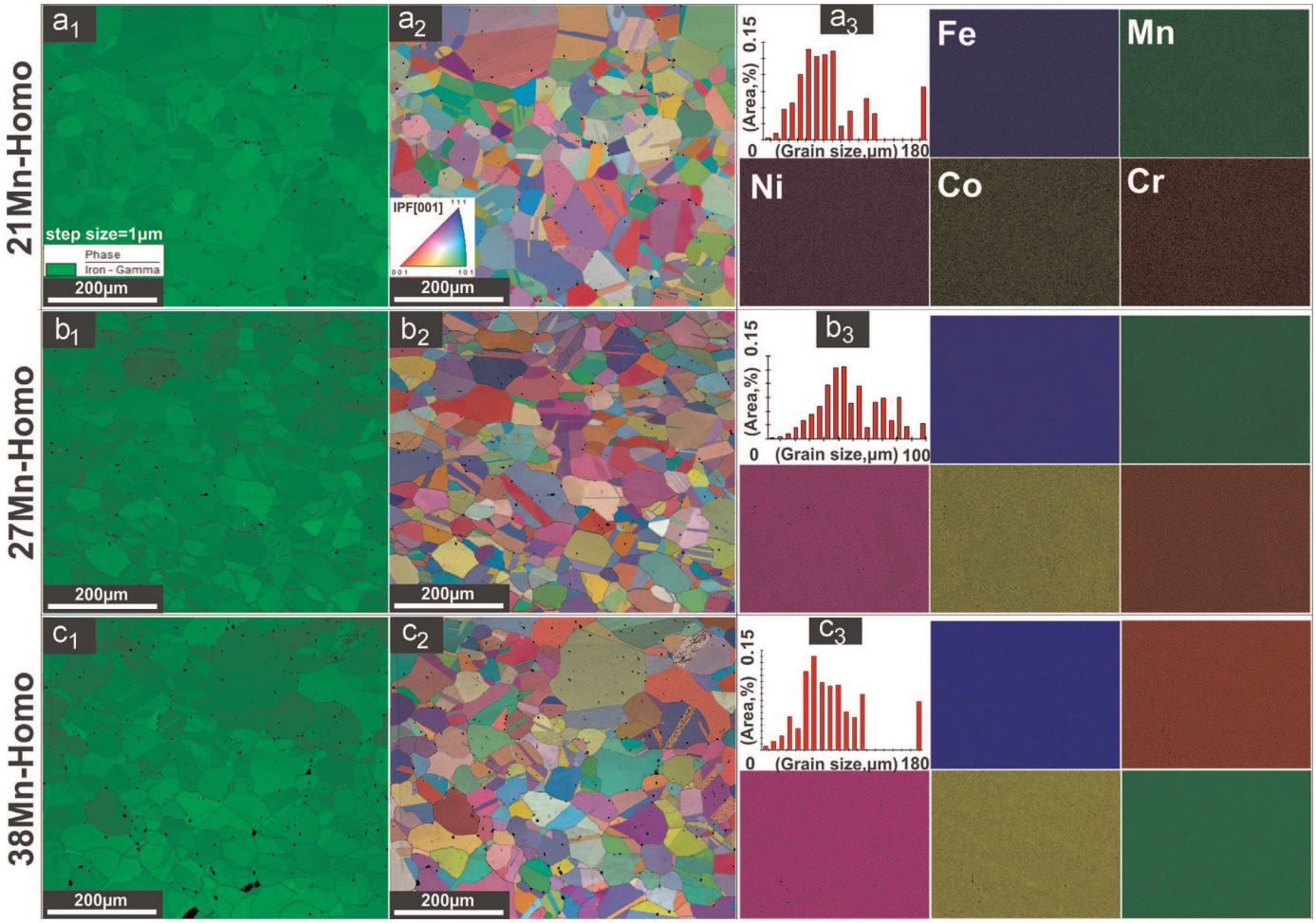

Fig. 3. EBSD phase maps of the homogenized state showing single fcc phase (with minor inclusion of MnO formed during casting); inverse pole figure maps with grain size distributions and EDX maps of all the elements corresponding to (a) 21Mn, (b) 27Mn and (c) 38Mn alloys.

no significant concentration fluctuation for the constituent elements and no chemical heterogeneities or decomposition across the GB (Fig. 4(f)). Similar APT observations have been reported earlier for grain interiors and at different GBs for the same alloy [21].

These observations verify that the introduced series of varying x-Mn alloy compositions are both structurally stable and chemically homogenous even after different processing steps. Hence, a single phase solid solution over a wide range of varying compositions has been successfully introduced.

3.2. Mechanical properties

3.2.1. Homogenized state

In order to understand the mechanical behavior of the introduced alloys, tensile tests were performed on all the different alloy compositions in their fully homogenized states. The average grain sizes (with twins excluded) for the alloys are 36.5 ± 28.5 μm, 42.7 ± 39.5 μm, 32.3 ± 23.7 μm, 33.0 ± 26.6 μm and 26.4 ± 30.1 μm, respectively with increasing Mn content. Fig. 5 (a) shows the representative engineering stress–strain curves for all alloys. In order to obtain statistically reliable results, a minimum of two to three tests were performed for each alloy and the results are summarized in Fig. 5(c).

Even though these x-Mn alloys exhibit a ~50% reduced yield strength (YS) and a corresponding 25–30% decrease in UTS compared to that of the equiatomic counterparts, they still exhibit outstanding ductility (similar to the equiatomic HEA for identical grain sizes [32]) (Fig. 5(a)) and strain-hardening ability (Fig. 5(b)). More interestingly, the mechanical response of all compositions is surprisingly similar. In fact, the uniform elongation (UE) of ~38% and the total elongation (TE) of ~58% remained identical while, the YS and ultimate tensile strength (UTS) show only a very gradual change (i.e. increase of ~15% and ~10% respectively) when the Mn concentration is increased by 17 at%. The strain-hardening behavior of all alloys is also similar with a sharp decrease in the strain hardening rate below 4% of true strain, and a more gradual decrease beyond 4% true strain. The hardness values (in Fig. 5(c)) follow a similar trend. The similarity of the mechanical response among the alloys (especially of the strain-hardening rates) indicates activity of similar deformation mechanisms in all alloys and limited influence of the Mn concentration on these mechanisms.

3.2.2. Cold rolled and recrystallized states

As observed in Fig. 5, the introduced series of non-equiatomic alloys possess excellent ductility and high strain-hardening ability. This enables tailoring of the properties through follow-up thermo-mechanical processing. To investigate the accessible property bounds, the 27Mn alloy was cold rolled to 64% thickness reduction. A sample of the cold rolled sheet was annealed at 900 °C for 10 min to achieve recrystallization and finer grain sizes compared to the homogenized state. These variants allow for the investigation of the influence of cold working and grain size reduction on the mechanical properties of the alloy system. Fig. 6((a1), (a2) and (b1),(b2)) shows the Kernel average misorientation (KAM) map

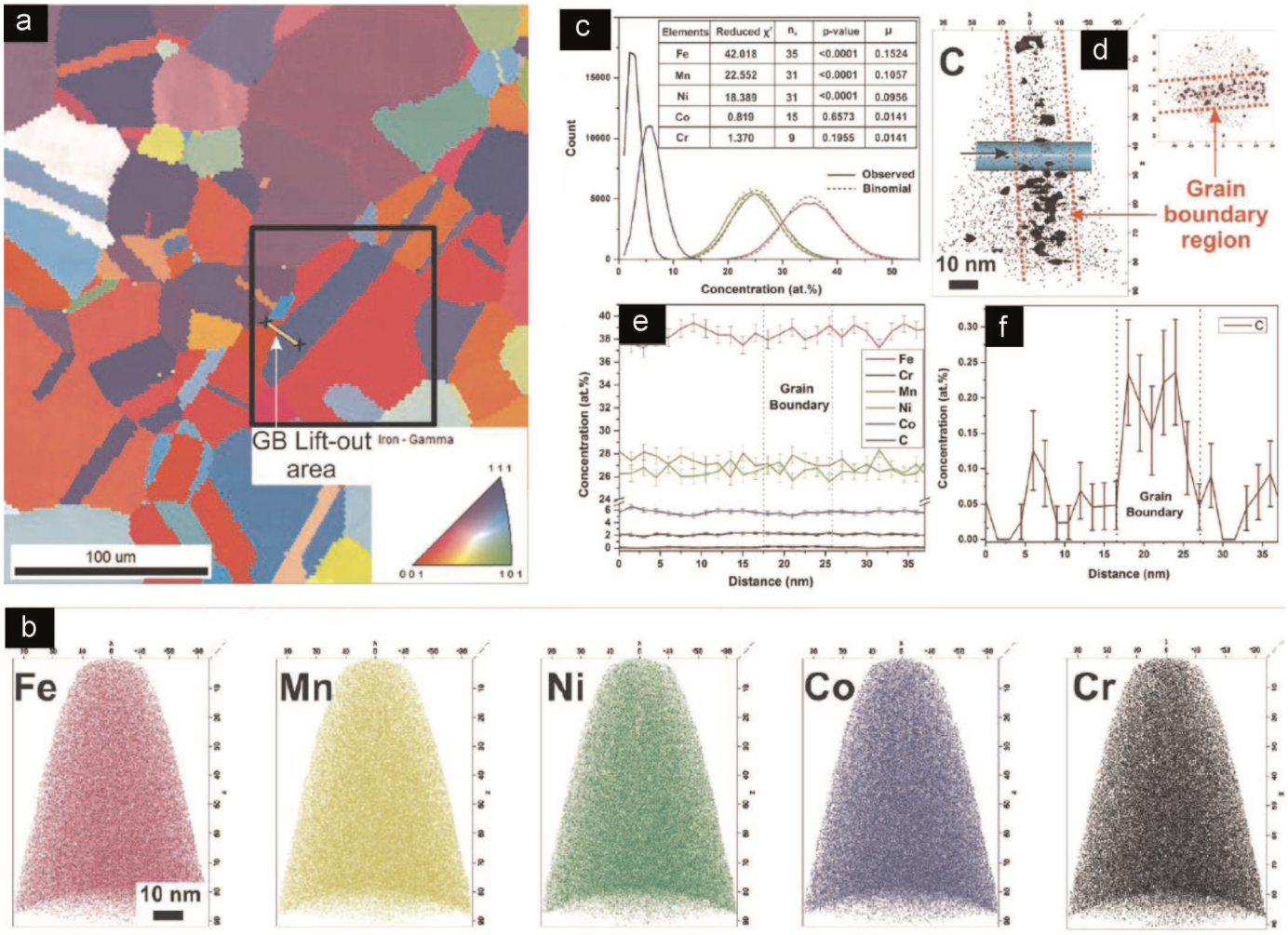

Fig. 4. Representative 27 Mn alloy microstructure in the homogenized state with (a) inverse pole figure map showing the grain boundary lift out region (indicated by white arrow inside the black rectangle). (b) Three-dimensional elemental maps of all constitutent elements together with their binomial frequency distribution analysis in (c). (d) Map of the impurity element carbon, with 0.1 at% isoconcentration surface, indicating its preferential segregation along the grain boundary (marked by red dotted lines both in cross section and top views). (e) 1D concentration profile of all elements (with carbon enlarged in (f)) taken along the cylinder of 10 nm diameter (in (d)) with 1.5 nm bin width. (For interpretation of the references to color in this figure legend, the reader is referred to the web version of this article.)

and the inverse pole figure (IPF) map of 64% cold rolled and subsequently heat treated samples (900 °C, 10 min) of 27Mn HEA variant. Heavily deformed areas within the grains and along the grain boundaries can be noticed in the cold rolled state. In spite of such heavy deformation the fcc solid solution remained stable and no second phase was observed [20]. The subsequent annealing treatment at 900 °C for 10 min resulted in the uniform recrystallization of deformed grains to an average grain size of about ~12 μm, excluding twin boundaries.

The tensile stress–strain curves corresponding to the 64% cold rolled and annealed states are shown in Fig. 5(a). The pre-deformation has introduced a high density of defects, resulting in a significant increase in the UTS to ~760 MPa but also a decrease in ductility to ~16%. This is related to the lack of strain hardening capacity, arising from the difficulty in further dislocation generation to sustain uniform deformation. On the other hand, annealing at 900 °C for 10 min recovers the ductility while also improving the strength (compared to the as-homogenized state) due to a pronounced Hall–Petch effect. The ~12.0 μm grain sized recrystallized state exhibits a ~150% increase in YS to ~240 MPa and a ~72% increase in UTS to ~645 MPa compared to that of the homogenized state with a grain size of ~32.3 μm. Hence, a strong Hall–Petch effect suggests that the GBs are very efficient in resisting shear transfer in addition to an effective reduction in the mean free path of dislocations which is inherent to HEAs.

3.2.3. *Deformation mechanism*

The pre-polished surface analysis of the tensile deformed 21Mn, 27Mn and 38Mn alloys is shown in Fig. 7 obtained at different strain levels of ~15% and ~50% respectively. The similarity of the surface deformation features confirms the expectation that all alloys considered in this study deform via the same deformation micro-mechanism. In each of the three cases shown here, at low strain levels fine surface steps are visualized on the deformed surface, often oriented differently in grains of different orientations but parallel within a grain as a group. Next to these are typical slip traces, and no signs of mechanical twinning is observed. At larger strains of ~15% (Fig. 7(a1)–(c1)) more groups of slip lines are observed inside most of the grains while at ~50% strain severe plastic flow and strong grain distortion can be observed. The slip lines are still visible in some grains but to a certain extent distorted due to the severe deformation.

The deformation sub-structure was further investigated in more detail by using ECCI for the 21Mn (Fig. 8(a)) and 38Mn (Fig. 8(b)) alloys as shown in Fig. 8. At ~1% strain (Fig. 8(a1)), dislocations form pile-up zones at GBs. This process results in the development of a typical planar slip substructure at ~5% strain (in both, the 21Mn and 38Mn alloys), with characteristic highly dense

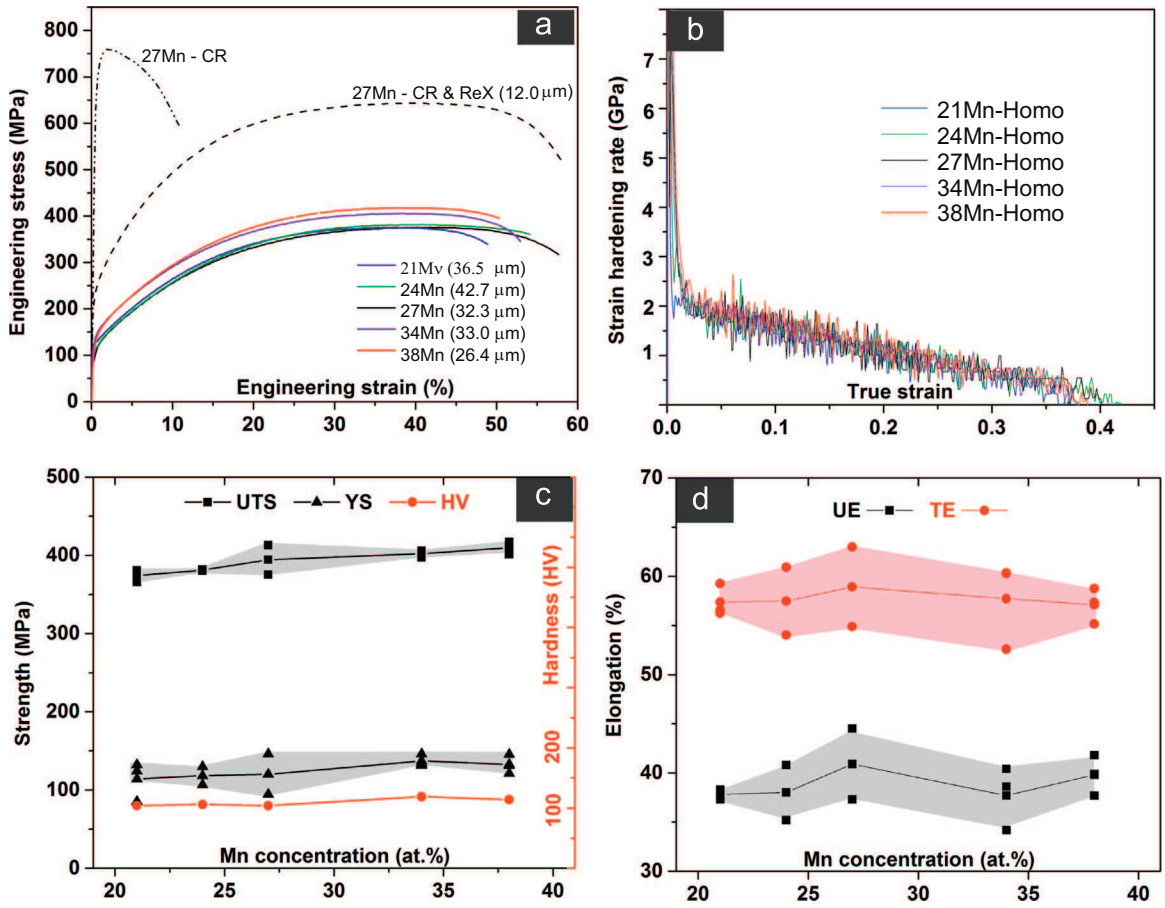

Fig. 5. (a) Stress–strain curves of all the alloys in their respective homogenized states, representative 27 Mn alloy both in cold rolled (64%) and recrystallized (900 °C, 10 min) states for comparison. (b) Strain hardening curves for all the x-Mn compositions (at%); (c) summary of yield strength (YS), ultimate tensile strength (UTS) and Vickers hardness (HV) as a function of Mn concentration and (d) summary of uniform (UE) and total elongation (TE) as a function of Mn concentration. The grain sizes of the respective states are shown in brackets in (a). CR: cold rolled; Rex: recrystallized.

dislocation walls (HDDWs) (see Fig. 8 (a2) and (b1)). In addition, dislocation cell structures are also observed at certain grains as shown in Fig. 8(a3) indicating the activation of wavy slip. At ~10% strain, strong interaction of HDDWs is observed for both investigated alloys (Fig. 8 (a4) and (b2)).

4. Discussion

The results clearly indicate that in order to form single phase solid solutions in multi-component materials, no indication was found that would justify confining HEA design strategies to equiatomic compositions. In fact, there are alloy systems for which a wide range of compositions may deliver similar microstructures. As proposed by Zhang et al. [24,35], in order to ensure formation of a single phase solid solution, the atomic size mismatch δ, should fulfill $\delta < 4.8$, and the absolute value of the enthalpy of mixing, ΔH_{mix} should lie within $-2.685\delta - 2.54 < \Delta H_{mix} < -1.28\delta + 5.44$ kJ mol^{-1}. Similarly, electronic parameters such as the valence electron concentration (VEC) and itinerant electron concentration (e/a) have been suggested to determine the structure and stability of solid solution alloys, similar to those recognized in the case of Hume-Rothery rules [26,27]. Accordingly, HEAs have been suggested to stabilize into bcc structure for VEC < 7.5 or $1.8 < e/a < 2.3$ whereas fcc structure develops for VEC > 7.5 or $1.6 < e/a < 1.8$. Zhang et al. later revised their solid solution formability condition to a double criterion: $\Omega \geq 1.1$ and $\delta \leq 6.6$, where Ω is defined as $\Omega = T_m{}^* \Delta S_{mix}/|\Delta H_{mix}|$ [25].

Table1 summarizes the above mentioned thermodynamic and electronic parameters calculated for the alloys introduced in this work and for the corresponding equiatomic composition, respectively. For the case of the introduced non-equiatomic alloy family, the ΔS_{config} values are significantly lower by 17–20% as compared to the equiatomic case. Moreover, the value of δ increases gradually with increasing Mn concentration, passing the critical δ value of 4.8 at 34Mn. Thus, according to the predictions of [24], a single phase solid solution should be ensured only for the 21Mn, 24Mn and 27Mn (where the less negative ΔH_{mix} help facilitate solid solution formation), while for compositions of x-Mn ($x \geq 30$) precipitation of the ordered phase inside a solid solution matrix may also be expected (due to the lower ΔH_{mix}). Such ordered precipitations have not been observed in the present case and instead all alloys exhibit random solid solutions under all processing conditions. While the double criterion in [25] successfully predicts solid solutions observed in this study, these considerations still raise ambiguities over the validity of a criteria based on ΔS_{config} solely governing solid solution formability in HEAs. Similar cases of non-equiatomic HEA compositions forming single phase solid solutions even though ΔS_{config} is not maximized were also reported elsewhere, together with the counter-example of other equi-atomic alloys exhibiting phase separation [20].

The calculated VEC (in Table 1) successfully predicts that the non-equiatomic alloys and the equiatomic HEA should exhibit stable fcc phase based on the above criteria. The e/a ratio based criteria, on the other hand, predict that only the equiatomic HEA can assume a stable fcc structure whereas the materials with

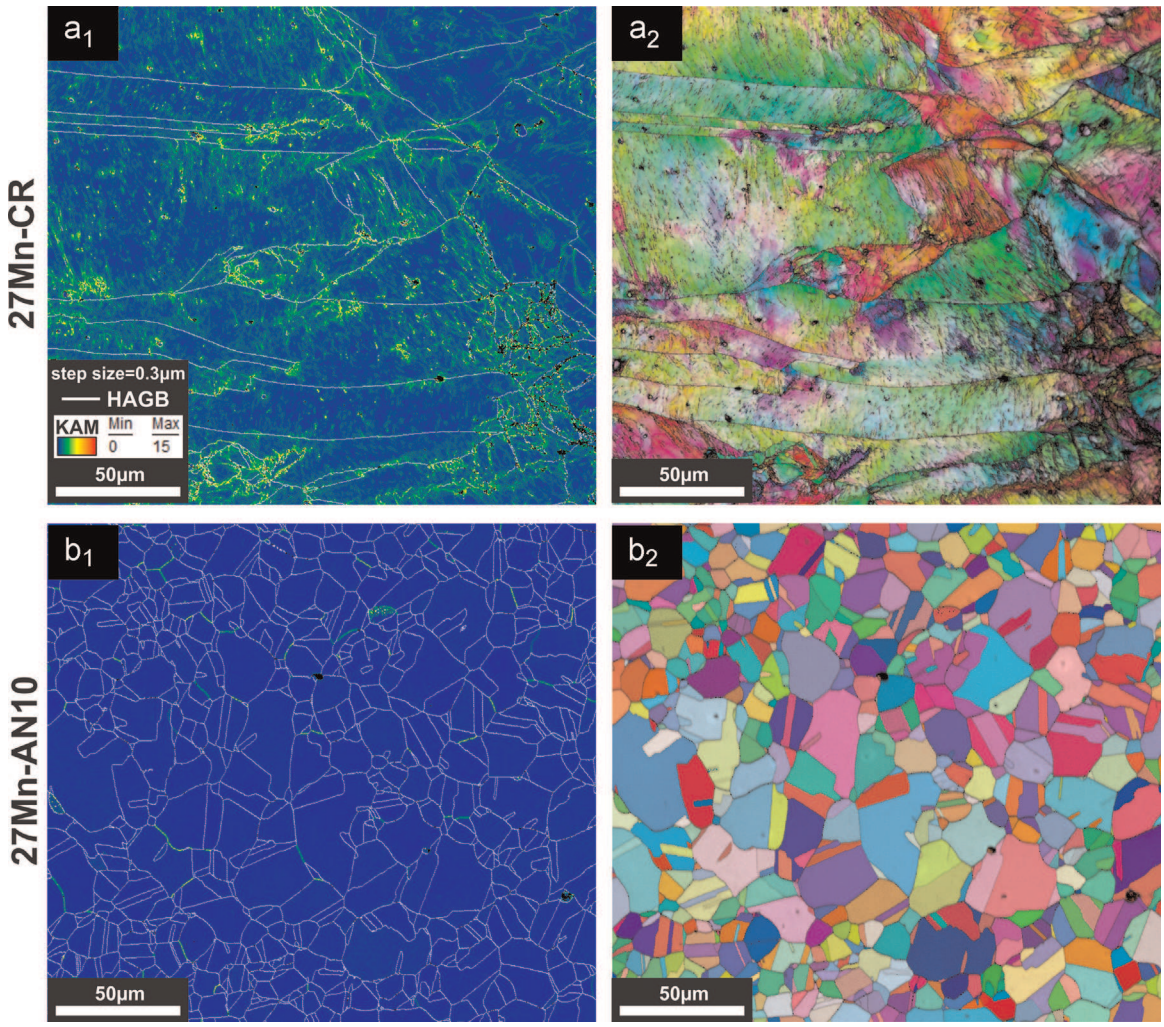

Fig. 6. EBSD Kernel average misorientation (KAM) and inverse pole figure (IPF) maps of the (a) cold rolled and (b) recrystallized states of the representative 27Mn alloy.

higher e/a ratios should crystallize in bcc structure. In [22] we report that Calphad predictions also suggest a bcc phase to co-precipitate in a fcc matrix at ~495 °C.

These conflicting results direct us towards a closer analysis on the role of kinetics. To this end, diffusion controlled kinetic calculations are performed using the DICTRA software with the database of MOBFE2 as shown in Fig. 9. The model is set such that an initially closed spherical fcc system of 1 μm diameter can precipitate a bcc phase when energetically favored (i.e. at 495 °C), with an incipient diameter of 0.5 nm. Fig. 9(a) shows that the as-formed bcc precipitate remains stable with a size of ~1.2 nm till apparent growth occurs after $\sim 10^7$ s i.e. ~115 days at 495 °C. Even after 3.2 years at 495 °C, the bcc precipitate can only reach a maximum size of 3.2 nm with a negligible volume fraction as indicated in Fig. 9(b). These observations suggest that the initially formed bcc nuclei shows very limited growth exhibiting kinetic freezing at room temperature and sluggish diffusion at slightly elevated temperatures of 495 °C. This result indicates that the HEA solidifies into a primary fcc phase and that sluggish kinetics freezes this state. Low atomic mobility and hence reluctance in growth and coarsening are plausible owing to the low intrinsic diffusion coefficients for HEAs. The reported observations of the appearance of Mn and Cr rich precipitations during high temperature deformation of the equiatomic FeCoNiCrMn HEA at lower strain rates of $\sim 10^{-4}\,s^{-1}$ supports this analysis [36].

The alloys exhibit similar tensile behavior as their equiatomic counterparts (Fig. 5), however with ~15% lower tensile strength [17]. This could be a result of the reduction in solid solution strengthening owing to the reduced amounts of Co and Cr present in the alloy. On the other hand the marginal 10–15% increase in YS and UTS with increasing Mn concentration can be attributed to the increasing atomic size misfit, δ as shown in Table 1. The increase in δ maximizes lattice distortion i.e. increase of friction stress on the dislocation motion resulting in a very marginal increase in strength [37]. Except for these very minimal effects on the increase in strengths, the strain hardening rates for all the x-Mn alloys are similar (in Fig. 5(b)) indicating that these alloys are deformed by similar mechanisms. However, the strong Hall–Petch effect, i.e. the increase in strength (~72%) upon decreasing grain sizes (from 50 μm down to 10 μm) observed for the case of the 27Mn alloy (in Fig. 5(a)) allows for further optimization of the mechanical properties by grain refinement. This is similar to the reported observations on the equiatomic HEA, where a significant improvement in YS and UTS were observed with reduction in grain size [32]. The deformation substructures observed in Fig. 8 also show similarities to those observed in austenitic steels and equiatomic HEAs [38]. Being a single phase solid solution, there are only few obstacles to dislocation motion and hence the major contribution to strain-hardening was observed to be caused by piling up of dislocations at grain boundaries at low strains ~1–2% (in Fig. 8 (a1)). In addition to the pile-up of dislocations at the early stages of plastic deformation, a strongly localized slip activity within a certain set of slip planes can be noticed. Considering the fact that the APT results (Fig. 4) shows no significant atomic clustering, it

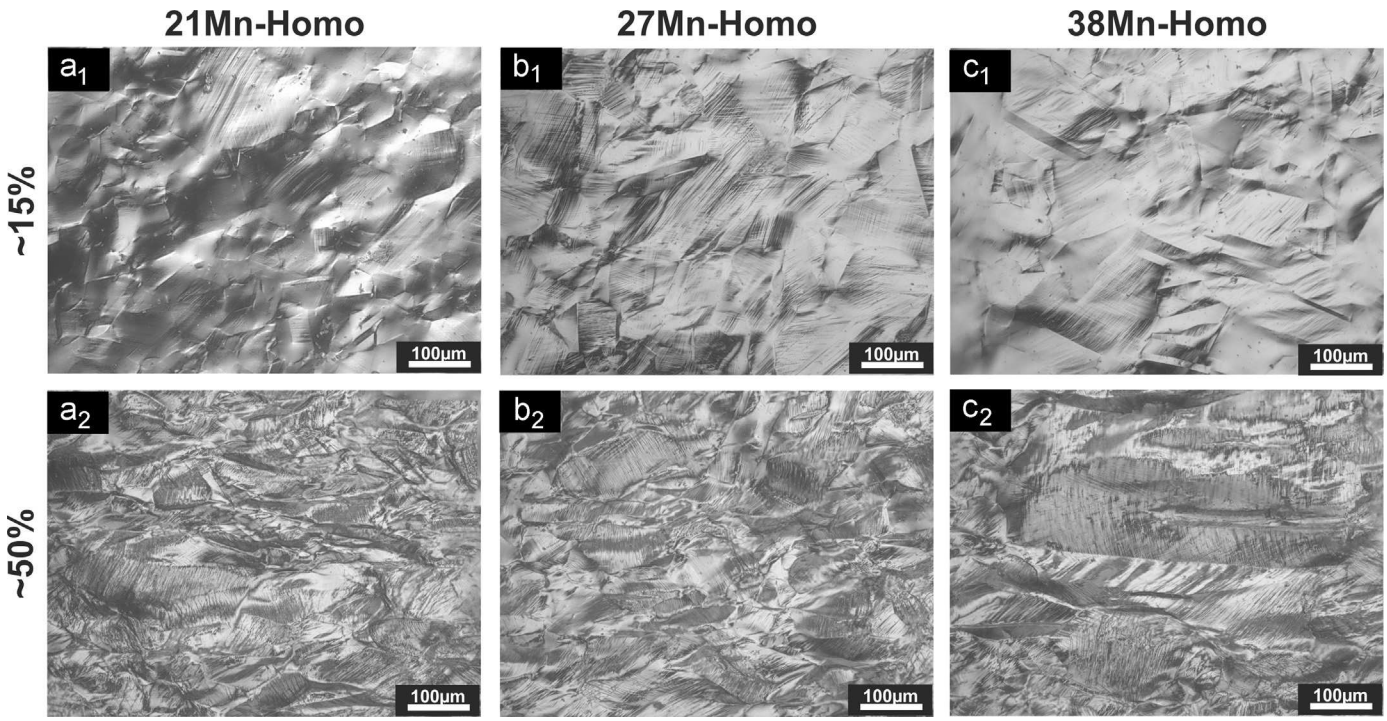

Fig. 7. Deformation microstructures obtained at strain levels of (a1, b1 and c1) 15% and (a2, b2 and c2) 50% as revealed by optical microscopy images for the representative 21Mn, 27Mn and 38Mn alloys.

can be presumed that the chances of local short range ordering being associated with dislocation glide on limited slip planes is negligible. Hence, the slip localization can be confirmed to be arising out of the frictional stress on dislocation motion due to lattice distortion [20]. At strains $>5\%$ both planar dislocation substructures (Fig. 8) with the inclusion of HDDWs and the dislocation cell structures arising out of wavy slip activity are visible in different grains. The observation of dislocation cell structures indicates that at higher strains more slip planes are activated accompanied by an increase in dislocation density facilitating frequent dislocation cross-slip. Very similar slip characteristics and intense dislocation substructure patterning were also observed in the highly alloyed low density FeMnC fcc steels [37,38].

5. Conclusions

A series of non-equiatomic FeMnNiCoCr high entropy alloys

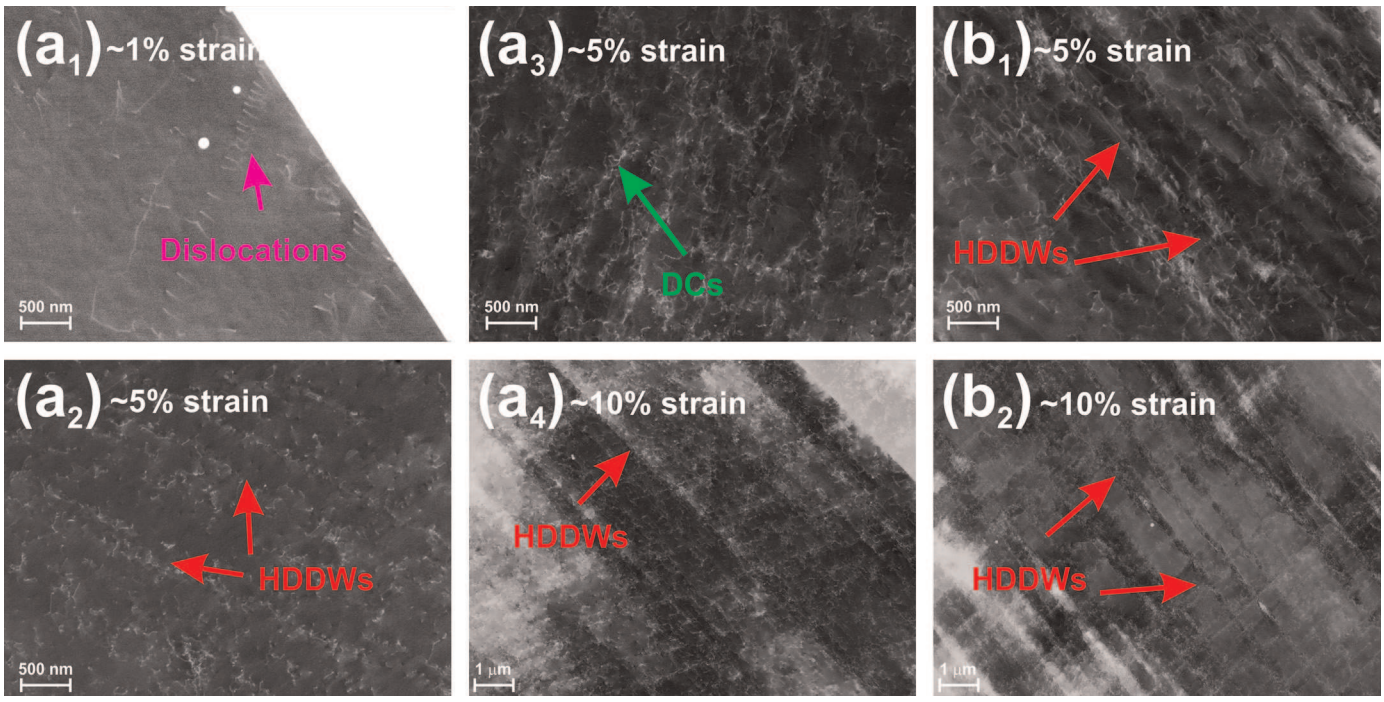

Fig. 8. Deformation substructures revealed by electron scanning contrast imaging for the representative (a) 21Mn and (b) 38Mn at different strain levels of 1%, 5% and 10%.

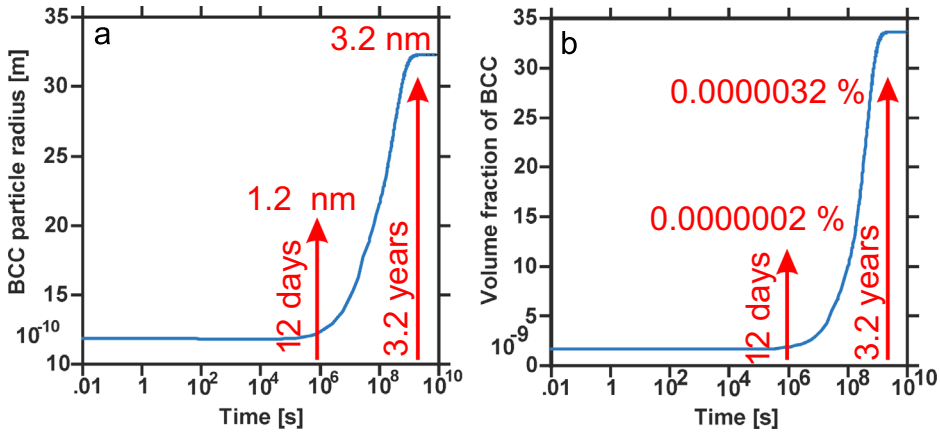

Fig. 9. DICTRA calculations predicting the nucleation and growth of a bcc structured particle in the $Fe_{32}Mn_{30}Ni_{30}Co_6Cr_2$ alloy at 495 °C as a function of time. Increase in size and volume fraction as a function of increasing holding time is shown respectively in (a) and (b). Even after 3.2 years at 495 °C, the bcc precipitate can only reach a maximum size of 3.2 nm with a negligible volume fraction of 32×10^{-7}%.

were successfully produced by rapid alloy prototyping RAP which were then hot rolled and homogenized to have equiaxed microstructures. XRD results of both the as-cast and homogenized states indicated the presence of a single phase, fcc structured solid solution with a lattice parameter of ~3.6 Å, also confirmed by EBSD phase maps. Microstructural characterization down to atomic resolution using APT showed no evidence of elemental partitioning or secondary phase formation neither in the grain interior nor at the grain boundaries. Also, DSC analyses indicated that the as-formed single phase solid solution remained stable up to their respective melting temperatures.

Mechanical characterization reveals that the introduced non-equiatomic HEAs have excellent tensile mechanical properties with the tensile strength increasing slightly with increasing Mn concentrations beyond 30 at%. However, the absolute values of yield and ultimate tensile strengths are slightly lower compared to those of their equiatomic counterparts. Deformation substructure investigation by ECCI revealed that the alloys exhibit a planar slip mode at lower strain levels of 1–2%. At higher strains (> 5%), HDDWs and cell structures were observed indicating more homogeneous slip. The observed room temperature deformation mechanisms are similar to those of the equiatomic alloy.

The structure formation and stability for a given composition as evaluated by their itinerant electron concentration values indicate that the current alloys are not expected to form a single phase fcc structure. Phase diagram and DICTRA calculations further support these estimates. Experimentally, however, a homogeneous fcc structure was observed owing to sluggish diffusion. Hence, we conclude that for forming a single phase solid solution, HEAs do not need to be strictly equiatomic. Instead, they can be tailored by exploiting wide ranges of non-equiatomic compositions with only slightly decreased configurational entropy. In other words, the minimization of the overall Gibbs free energy should be the critical alloy design criterion and not the maximization of the configurational entropy alone. The current HEA design criteria have only led to the discovery of very few successful single phase solid solutions. Alternatively, when focusing on the design of the non-equiatomic HEAs a much wider range of single phase solid solution strengthened alloys for extreme conditions can be explored and developed.

Acknowledgments

The authors gratefully acknowledge the funding by the European Research Council under the EU's 7th Framework Programme (FP7/2007–2013))/ERC Grant agreement 290998 "SmartMet".

References

[1] J.W. Yeh, S.K. Chen, S.J. Lin, J.Y. Gan, T.S. Chin, T.T. Shun, C.H. Tsau, S.Y. Chang, Nanostructured high-entropy alloys with multiple principal elements: novel alloy design concepts and outcomes, Adv. Eng. Mater. 6 (2004) 299–303.
[2] J.-W. Yeh, S.-J. Lin, T.-S. Chin, J.-Y. Gan, S.-K. Chen, T.-T. Shun, C.-H. Tsau, S.-Y. Chou, Formation of simple crystal structures in Cu–Co–Ni–Cr–Al–Fe–Ti–V alloys with multiprincipal metallic elements, Metall. Mater. Trans. A 35 (2004) 2533–2536.
[3] B. Cantor, I.T.H. Chang, P. Knight, A.J.B. Vincent, Microstructural development in equiatomic multicomponent alloys, Mater. Sci. Eng. A 375–377 (2004) 213–218.
[4] S. Ranganathan, Alloyed pleasures: multimetallic cocktails, Curr. Sci. 85 (2003) 1404–1406.
[5] K.G. Pradeep, N. Wanderka, P. Choi, J. Banhart, B.S. Murty, D. Raabe, Atomic-scale compositional characterization of a nanocrystalline AlCrCuFeNiZn high-entropy alloy using atom probe tomography, Acta Mater. 61 (2013) 4696–4706.
[6] C.C. Tung, J.W. Yeh, T.T. Shun, S.K. Chen, Y.S. Huang, H.S. Chen, On the elemental effect of AlCoCrCuFeNi high-entropy alloy system, Mater. Lett. 61 (2007) 1–5.
[7] Y. Zhang, T.T. Zuo, Z. Tang, M.C. Gao, K.A. Dahmen, P.K. Liaw, Z.P. Lu, Microstructures and properties of high-entropy alloys, Prog. Mater. Sci. 61 (2014) 1–93.
[8] A. Manzoni, H. Daoud, R. Völkl, U. Glatzel, N. Wanderka, Phase separation in equiatomic AlCoCrFeNi high-entropy alloy, Ultramicroscopy 132 (2013) 212–215.
[9] F. Otto, Y. Yang, H. Bei, E.P. George, Relative effects of enthalpy and entropy on the phase stability of equiatomic high-entropy alloys, Acta Mater. 61 (2013) 2628–2638.
[10] S. Singh, N. Wanderka, B. Murty, U. Glatzel, J. Banhart, Decomposition in multi-component AlCoCrCuFeNi high-entropy alloy, Acta Mater. 59 (2011) 182–190.
[11] X. Xu, P. Liu, S. Guo, A. Hirata, T. Fujita, T. Nieh, C. Liu, M. Chen, Nanoscale phase separation in a fcc-based CoCrCuFeNiAl 0.5 high-entropy alloy, Acta Mater. 84 (2015) 145–152.
[12] J.-W. Yeh, Alloy design strategies and future trends in high-entropy alloys, J. Miner. Met. Mater. Soc. 65 (2013) 1759–1771.
[13] O. Senkov, G. Wilks, D. Miracle, C. Chuang, P. Liaw, Refractory high-entropy alloys, Intermetallics 18 (2010) 1758–1765.
[14] B. Cantor, Multicomponent and high entropy alloys, Entropy 16 (2014) 4749–4768.
[15] K.B. Kim, P.J. Warren, B. Cantor, Glass-forming ability of novel multicomponent (Ti33Zr33Hf33)–(Ni50Cu50)–Al alloys developed by equiatomic substitution, Mater. Sci. Eng.: A 375–377 (2004) 317–321.
[16] K.B. Kim, Y. Zhang, P.J. Warren, B. Cantor, Crystallization behaviour in a new multicomponent Ti16 · 6Zr16 · 6Hf16 · 6Ni20Cu20Al10metallic glass developed by the equiatomic substitution technique, Philos. Mag. 83 (2003) 2371–2381.
[17] A. Gali, E.P. George, Tensile properties of high- and medium-entropy alloys, Intermetallics 39 (2013) 74–78.
[18] B. Gludovatz, A. Hohenwarter, D. Catoor, E.H. Chang, E.P. George, R.O. Ritchie., A fracture-resistant high-entropy alloy for cryogenic applications, Science 345 (2014) 1153–1158.
[19] Y. Deng, C. Tasan, K. Pradeep, H. Springer, A. Kostka, D. Raabe, Design of a twinning-induced plasticity high entropy alloy, Acta Mater. 94 (2015)

124–133.
[20] C.C. Tasan, Y. Deng, K.G. Pradeep, M.J. Yao, H. Springer, D. Raabe, Composition dependence of phase stability deformation mechanisms, and mechanical properties of the CoCrFeMnNi high-entropy alloy system, J. Miner. Met. Mater. Soc. 66 (2014) 1993–2001.
[21] M.J. Yao, K.G. Pradeep, C.C. Tasan, D. Raabe., A novel, single phase, non-equiatomic FeMnNiCoCr high-entropy alloy with exceptional phase stability and tensile ductility, Scr. Mater. 72–73 (2014) 5–8.
[22] D. Ma, M. Yao, K.G. Pradeep, C.C. Tasan, H. Springer, D. Raabe, Phase stability of non-equiatomic CoCrFeMnNi high entropy alloys, Acta Mater. 98 (2015) 288–296.
[23] H. Springer, M. Beide, D. Raabe., Bulk combinatorial design of ductile martensitic stainless steels through confined martensite-to-austenite reversion, Mater. Sci. Eng. A 582 (2013) 10.
[24] Y. Zhang, Y.J. Zhou, J.P. Lin, G.L. Chen, P.K. Liaw, Solid-solution phase formation rules for multi-component alloys, Adv. Eng. Mater. 10 (2008) 534–538.
[25] X. Yang, Y. Zhang, Prediction of high-entropy stabilized solid-solution in multi-component alloys, Mater. Chem. Phys. 132 (2012) 233–238.
[26] S. Guo, C. Ng, J. Lu, C. Liu, Effect of valence electron concentration on stability of fcc or bcc phase in high entropy alloys, J. Appl. Phys. 109 (2011) 103505.
[27] M.G. Poletti, L. Battezzati, Electronic and thermodynamic criteria for the occurrence of high entropy alloys in metallic systems, Acta Mater. 75 (2014) 297–306.
[28] H. Springer, D. Raabe, Rapid alloy prototyping: compositional and thermo-mechanical high throughput bulk combinatorial design of structural materials based on the example of 30Mn–1.2C–xAl triplex steels, Acta Mater. 60 (2012) 4950–4959.
[29] S. Mandal, K.G. Pradeep, S. Zaefferer, D. Raabe., A novel approach to measure grain boundary segregation in bulk polycrystalline materials in dependence of the boundaries' five rotational degrees of freedom, Scr. Mater. 81 (2014) 16–19.
[30] I. Gutierrez-Urrutia, S. Zaefferer, D. Raabe, Electron channeling contrast imaging of twins and dislocations in twinning-induced plasticity steels under controlled diffraction conditions in a scanning electron microscope, Scr. Mater. 61 (2009) 737–740.
[31] S. Zaefferer, N.-N. Elhami, Theory and application of electron channelling contrast imaging under controlled diffraction conditions, Acta Mater. 75 (2014) 20–50.
[32] F. Otto, A. Dlouhý, C. Somsen, H. Bei, G. Eggeler, E.P. George., The influences of temperature and microstructure on the tensile properties of a CoCrFeMnNi high-entropy alloy, Acta Mater. 61 (2013) 5743–5755.
[33] N. Mattern, J. Han, K. Pradeep, K. Kim, E. Park, D. Kim, Y. Yokoyama, D. Raabe, J. Eckert, Structure of rapidly quenched (Cu 0.5 Zr 0.5) 100 − xAgx alloys (x=0–40 at%), J. Alloy. Compd. 607 (2014) 285–290.
[34] M.P. Moody, L.T. Stephenson, A.V. Ceguerra, S.P. Ringer, Quantitative binomial distribution analyses of nanoscale like-solute atom clustering and segregation in atom probe tomography data, Microsc. Res. Tech. 71 (2008) 542–550.
[35] Y. Zhang, Z. Y. Jeju, 2007, p. 3.
[36] J. He, C. Zhu, D. Zhou, W. Liu, T. Nieh, Z. Lu, Steady state flow of the FeCoNiCrMn high entropy alloy at elevated temperatures, Intermetallics 55 (2014) 9–14.
[37] I. Gutierrez-Urrutia, D. Raabe, Dislocation and twin substructure evolution during strain hardening of an Fe–22 wt% Mn–0.6 wt% C TWIP steel observed by electron channeling contrast imaging, Acta Mater. 59 (2011) 6449–6462.
[38] I. Gutierrez-Urrutia, D. Raabe., Multistage strain hardening through dislocation substructure and twinning in a high strength and ductile weight-reduced Fe–Mn–Al–C steel, Acta Mater. 60 (2012) 5791–5802.